

Three-dimensional topological plasmons in Weyl semimetalsFuru Zhang , Yang Gao, and Wei Zhang *Institute of Applied Physics and Computational Mathematics, Beijing 100088, China*

(Received 9 October 2020; revised 17 November 2021; accepted 17 November 2021; published 29 November 2021)

Our systematic studies on the topological aspects of plasmons of Weyl semimetals in the presence of a magnetic field have uncovered two types of three-dimensional (3D) topological plasmons: the bulk plasmons and the Fermi-arc plasmons over opposite surfaces. As a consequence of the bulk-boundary correspondence, there are unidirectional surface/edge plasmons whose directions and dispersions can be controlled by the external field. These chiral surface plasmons possess momentum-location lock and strong confinement of electromagnetic (EM) fields. The anomalous Hall conductivity brings about abundant anisotropic plasmon dispersions, from linear to parabolic or even hyperbolic bands. In addition, a semiclassical picture of electron motion is proposed to show the formation of Weyl orbits and the consequent effect on plasmons. Our work thus provides instructive insights into the electron dynamics and collective excitations of Weyl semimetals and suggests it is a good seed for 3D topological plasmonics.

DOI: [10.1103/PhysRevB.104.205141](https://doi.org/10.1103/PhysRevB.104.205141)**I. INTRODUCTION**

In recent years there have been extensive studies on the electronic and optical properties of graphene and topological Dirac/Weyl semimetals [1–13]. The topological Dirac and Weyl semimetals are both three-dimensional (3D) analogs of graphene with linear low energy excitations, which behave like Dirac and Weyl fermions in quantum field theory. The topological band structure of Weyl semimetals (with broken time-reversal symmetry and/or broken inversion symmetry) leads to the magnetic monopoles in momentum space and topologically protected Fermi arcs on surfaces [14–16]. In addition to the theoretical predictions [17–19], there have been several experiments proposed for realizing Weyl semimetals in real materials [20–23]. The Weyl nodes in the bulk and the Fermi arcs on the surface have been observed in TaAs [20–23].

Nontrivial physics of Weyl semimetals comes from the linear dispersion of 3D systems and topological band structure. The linear dispersion leads to strong nonlinear optical response [24,25] and electronic transport [26]. Many interesting physics effects spring up as a consequence of band topology, such as chiral magnetic effect, axion electrodynamics, nonlinear Hall effect, and chiral anomaly related unusual magnetotransport [27–38]. Because of the Berry flux between Weyl nodes, Weyl semimetal owns a 3D anomalous Hall effect and the intrinsic Hall conductivity is proportional to the distance between Weyl nodes [39,40]. Importantly, the Fermi arcs and chiral zeroth Landau levels (LLs) will form closed Weyl orbits [41–43], giving rise to a unique 3D quantum Hall effect [44,45]. Whereas the relationship between Weyl orbits and the Berry curvature of Fermi arcs is not known, nor is the velocity of the electron tunneling between surfaces.

Furthermore, what is the impact of Weyl orbits on the collective excitations? Our studies in this work make a step in the research on these interesting topics.

Weyl semimetal can serve as a potential optical material with electromagnetic response described by a topological Chern-Simon term. Many aspects of the optical properties of Weyl semimetals, in particular plasmons (the collective excitations of Weyl electrons), have been studied extensively [46–70]. The plasmon hybridization induced short-range surface plasmons and long-range surface plasmons in thin-film Weyl semimetals have been addressed in [48]. Plasmons in Weyl semimetals TaAs/NbAs and MoTe₂ have been investigated by electron energy loss spectroscopy (EELS) [50,51], which is consistent with optical measurements [52–54]. The coupling effects of surface plasmons/Fermi arc plasmons in Weyl semimetals have been explored in [56], where it has been found that coupling increases the lifetime of the surface plasmon mode. It has been pointed out that the plasmon modes in Weyl semimetals are anisotropic and expected to have an experimental signature [57]. The frequency of the bulk Weyl plasmons depends on the position of Fermi surface and is related to the chiral anomaly [58,59]. Due to the effective magnetic field in momentum space, the surface Weyl plasmons are similar to magnetoplasmons in ordinary metals [60,61]. The Fermi-arc plasmons are chiral and own a linear dispersion, which implies the Fermi-arc electron liquid is a unique one lying in between the one-dimensional (1D) and two-dimensional (2D) electron liquids [62–64]. In the presence of a magnetic field, plasmons in Weyl semimetals earn more interesting optical properties, such as chiral electric separation, coupling-induced transparency, and nonclassical density response [65–67]. However, there is no discussion about nontrivial topology of Weyl plasmons, nor influence of the “wormhole” tunneling on the plasmon property.

In this work we investigate the magnetoplasmonics in Weyl semimetals, focusing on magnetic-field tunable topological

*zhang_wei@iapcm.ac.cn

properties. We point out that the bulk Weyl magnetoplasmons and the Fermi-arc magnetoplasmons over opposite surfaces are both 3D topological plasmons. Consistent with the non-trivial topology of the bulk (surface) states, there are novel unidirectional surface (edge) plasmons whose direction and dispersion can be controlled by the external field. These chiral surface plasmons own momentum-location lock and are mixed with the bulk LL plasmons. The anomalous Hall conductivity could influence the magnetoplasmon dispersion greatly, resulting in linear (gapless), parabolic, or even hyperbolic (gapped) bands. Strong confinement of the EM field associated with the Fermi-arc plasmons can be achieved. We also propose a semiclassical picture of the formation of Weyl orbits, connecting the opposite Fermi-arc plasmons into a whole one. Our work thus sheds some new light on the electron dynamics and collective excitations of Weyl semimetals and proposes potential applications of Weyl semimetals in 3D chiral and topological plasmonics.

II. MODEL OF WEYL SEMIMETALS

To illustrate the properties of plasmons in the presence of a uniform magnetic field $\mathbf{B} = (0, B, 0)$, we start from a minimal model of Weyl semimetals [71]:

$$H = A(k_x\sigma_x + k_y\sigma_y) + M(b^2 - k^2)\sigma_z + D_1k_y^2 + D_2k_{\parallel}^2, \quad (1)$$

which breaks the time-reversal symmetry and hosts a pair of Weyl nodes at $(0, 0, \pm b)$. $\mathbf{k} = (k_x, k_y, k_z)$ and $k_{\parallel}^2 = k_x^2 + k_z^2$. The effective model for the Fermi arc at the top ($\tau = 1$) or bottom ($\tau = -1$) surface reads [44]:

$$h_{\tau} = \tau vk_x + (D_2 - D_1)k_{\parallel}^2 + D_1b^2, \quad (2)$$

where $v = A\sqrt{M^2 - D_1^2}/M$. The anisotropic parameters D_1 and D_2 make the Fermi arc a two-dimension (2D) dispersion. The Fermi level lying at the Weyl nodes is $E_F = D_2b^2$. At the top surface, the Fermi-arc electrons ($k_x > 0$) have a positive velocity ($\partial h_{\tau}/\partial k_x$) propagating along the x direction; oppositely, the electron velocity is negative at the bottom surface ($k_x < 0$).

The Weyl semimetal may have a large anomalous Hall conductivity [72,73]. For any $k_z \in (-b, b)$, there is a well defined Chern number $C_{k_z} = \text{sgn}(M)$ [39] in the conduction band which is related to the existence of the Fermi arcs. As a result, the anomalous Hall conductivity is proportional to the distance between Weyl nodes: $\sigma_H = \sigma_{yx} = \text{sgn}(M)\frac{e^2}{2\pi\hbar}2b$ [39,40]. With an applied magnetic field, the bulk conductivity $\hat{\sigma}$ and the surface conductivity σ^s will take changes accordingly (see Appendix A for details). In this paper we focus on the topological plasmons in type-I Weyl semimetals. Type-II Weyl semimetals have a different structure of Fermi surface and different anomalous Hall conductivity than those of type-I Weyl semimetals, which have important impact on the topological plasmons (see next section).

III. CHIRAL SURFACE PLASMONS

Below we will give a detailed investigation of the surface plasmons in Weyl semimetals, and we shall focus on the undoped case. We start from the electrodynamic equations of

the Weyl electrons. We assume the thickness of the slab L is very large and the electric potential near the top surface ($y = 0$) takes the form as $\phi(x, y < 0, z) = \phi_0 e^{ky} e^{i(q_z z + q_x x - \omega t)}$ (discussions about plasmons on the right and front surfaces can be seen in Appendixes C and D). Accordingly, the electric field $\mathbf{E} = -\nabla\phi$, the charge density ρ , and the current density \mathbf{j} hold the same form. From the Poisson equation $\nabla^2\phi = -\rho/\epsilon_0\epsilon\Theta(-y)$, the charge conservation equation $\frac{\partial\rho}{\partial t} + \nabla\cdot\mathbf{j} = 0$, and the microscopic Ohm's law $\mathbf{j} = \hat{\sigma}\mathbf{E}$, we obtain the bulk relationship (see Appendix B 1):

$$\epsilon_0\epsilon(q^2 - k^2) = \frac{\eta k(q_z + iq_x)\sigma_H}{i\omega(1 - \eta^2)}, \quad (3)$$

where $q = \sqrt{q_x^2 + q_z^2}$ and $\eta = \omega_c/\omega$ with a cyclotron frequency ω_c . ϵ_0 is the permittivity of vacuum, and $\epsilon = 13$ is the static dielectric constant of the medium [52]. Instead of the topological Chern-Simon term modifying the Maxwell's equations, the information of the topology of Weyl electrons here is completely described by the anomalous Hall conductivity σ_H .

At the top surface, the boundary condition gives the constitutive relation which determines the Fermi-arc plasmon dispersions:

$$\epsilon_0(q + \epsilon k) = \frac{q_x\sigma_H}{\omega} + \frac{q_z^2\sigma_{zz}^s + q_x^2\sigma_{xx}^s + iq_z q_x \eta(\sigma_{zz}^s - \sigma_{xx}^s)}{i\omega(1 - \eta^2)}, \quad (4)$$

where σ_{jj}^s is the surface conductivity which can be calculated by the Hamiltonian Eq. (2) of the surface states or by defining from the bulk conductivity as $\sigma^s = \sigma_{\text{bulk}}L$ [44]. Theoretical derivation suggests that $\sigma_{jj}^s = \alpha\epsilon_0\tilde{\sigma}_{jj}^s \approx \alpha\epsilon_0\frac{iD_j}{\omega - vq_x}$ where $\alpha = e^2/h\epsilon_0$ and D_j is the Drude weight in the AC conductivity (see Appendixes B 3 and B 4).

For the intrinsic case $\omega_c = 0$, if $\sigma_H \rightarrow 0$ and $\omega \gg vq_x$, one obtains the traditional 2D plasmon whose frequency is proportional to \sqrt{q} : $\omega = \sqrt{\alpha D_0 q / 2\epsilon_{\text{eff}}}$, where $D_z = D_x = D_0$, $\epsilon_{\text{eff}} = (1 + \epsilon)/2$. In general, Eq. (4) indicates anisotropic Fermi-arc plasmons in accordance with the anisotropy in the Fermi-arc dispersion. For the z direction, $\omega = \sqrt{\alpha D_z q_z / 2\epsilon_{\text{eff}}}$; for the x direction, in the low frequency range $\omega \ll \alpha\tilde{\sigma}_H$ where $\tilde{\sigma}_H = \sigma_H/\alpha\epsilon_0$, one can get a linear plasmon $\omega = (v - D_x/\tilde{\sigma}_H)q_x$, which is consistent with the result utilizing 3D dielectric function [64]. The anisotropic plasmon dispersion results in different EM responses for external fields with different polarization. Unlike the case with polarization along z direction, the plasmonic modes with $q_z = 0$ cannot be excited directly due to $v/\hbar < c$, just as the usual surface plasmon at the interface between metal and vacuum.

When the external magnetic field is applied, a gap will be opened in the plasmon dispersion [74,75]. If $\sigma_H \rightarrow 0$, $\omega \gg vq_x$, one can get the traditional 2D magnetoplasmon $\omega = \sqrt{\frac{\alpha D_0 q}{2\epsilon_{\text{eff}}} + \omega_c^2}$. If $\tilde{\sigma}_H \gg \omega/\alpha$ and $q_x = 0$, the constitutive relations suggest that $\text{Re}[k] \ll q_z$. In the long wave limit $q_z \rightarrow 0$, Eq. (4) gives a novel gapped mode $\omega = \sqrt{\alpha D_z |q_z|} + \omega_c^2$, which differs from the traditional magnetoplasmon.

In the x direction, the magnetic field and the anomalous Hall conductivity bring about plasmon dispersions.

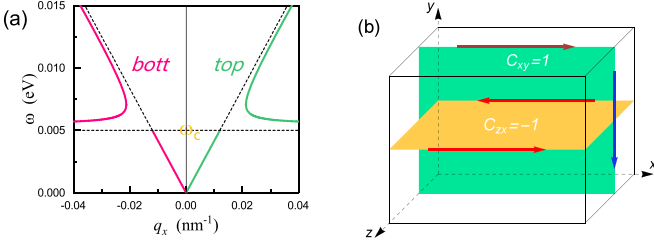


FIG. 1. (a) Dispersion of Weyl surface plasmons on the top and bottom surfaces. $D_x = 0.05$ eV, $q_z = 0$, $\hbar\omega_c = 5$ meV, $v = 0.5$ eV nm, $\tilde{\sigma}_H = 0.6$. The dashed lines denote the dispersions of $\omega = \pm(v - D_x/\tilde{\sigma}_H)q_x$ and $\omega = \omega_c$. (b) Schematic diagrams of the propagation of the surface plasmons and the corresponding bulk topology. See Appendixes C and D for discussions about plasmons on the right and front surfaces.

In the long wave limit $q_x \rightarrow 0$ we have

$$\omega = (v - D_x/\beta\tilde{\sigma}_H)q_x, \quad (5)$$

as plotted in Fig. 1(a). When $\omega_c = 0$, it turns back into the intrinsic mode with $\beta = 1$. While in the limit $\omega_c \rightarrow +\infty$ we have $\beta \rightarrow +\infty$ and $\omega = vq_x$ (see Appendix C 5). It is also a gapless linear magnetoplasmon. Because $\omega \geq 0$, one obtains $q_x \geq 0$ implying that it propagates unidirectionally only along the positive x direction. These properties are significantly different from the traditional surface magnetoplasmons which are gapped. In the next section we will show that it is a surface counterpart of the topological bulk plasmon.

When $\omega \gtrsim \omega_c$, from Eq. (3) we have $k \approx 0$. If $\tilde{\sigma}_H \gg \omega/\alpha$, from Eq. (4) one can get that ($q_z = 0$)

$$\left(1 - \frac{\omega_c^2}{\omega^2}\right) \left(1 - \frac{\omega}{vq_x}\right) = \frac{D_x}{v\tilde{\sigma}_H}, \quad (6)$$

which gives an unusual plasmon with a hyperbolic band. Let the right side be zero ($D_x = 0$), we get the equations of two asymptotes $\omega_1 = vq_x$ and $\omega_2 = \omega_c$. In the limit $\omega/\omega_c \rightarrow +\infty$, Eq. (6) gives the intrinsic dispersion that $\omega = (v - D_x/\tilde{\sigma}_H)q_x$. The exact solution is plotted in Fig. 1(a). From the dispersion relationship one can obtain $q_x \geq \frac{\omega_c}{v} (1 + \sqrt{2D_x/v\tilde{\sigma}_H}) \equiv \bar{q}$ for the branch $\omega \geq \omega_c$. Then in the real space there is a confinement of the EM field associated with the Fermi-arc plasmon. The maximum confinement length $1/\bar{q}$ can be tuned by the external magnetic field. This is quite different from the case in intrinsic plasmons or traditional magnetoplasmons. This peculiar dispersion and confinement of EM field are (partially) due to the anomalous Hall current that connects the bulk and surface degrees of freedom (see Appendix B 2). These plasmons with different dispersions could be observed in experiment. Some features of plasmons, such as anisotropic dispersion and dispersion proportional to \sqrt{q} (for intrinsic case) in topological materials, have been explored in recent studies [57,76,77].

It is worth noting that in Fig. 1(a) the plasmon momentum q_x is locked with its surface location. This is a result due to the particular way of electron transitions in Fermi arcs. For the top Fermi arc, the electrons with dispersion $\hbar\tau_{=1} \approx vk_x$ can only absorb the photons whose momentum is positive; but for the bottom surface, the photons' momentum must be negative. Here we would like to note that the inclusion of

scattering from defects/impurities in real materials leads to finite lifetime of plasmons. Yet, the basic physical picture remains unchanged (see Appendix B 8 for detailed calculations and discussions). In the next section we will show that it is also a result from the nontrivial bulk topology.

IV. TOPOLOGICAL BULK PLASMONS

Below we will point out that the Weyl semimetal can host a 3D topological plasmon with the help of the magnetic field, and the unidirectional surface plasmons can be classified according to the topology of the bulk.

We come from the set that $\phi(\mathbf{r}) = \phi_0 e^{i(q_x x + q_y y + q_z z - \omega t)}$ and $\rho(\mathbf{r}) = \rho_0 e^{i(q_x x + q_y y + q_z z - \omega t)}$. The electrodynamic equations give the constitutive relation that

$$\epsilon_0 \epsilon q^2 = \frac{\omega_c q_y \sigma_H (q_z + i\eta q_x)}{\omega^2 - \omega_c^2}. \quad (7)$$

Here $q = \sqrt{q_x^2 + q_y^2 + q_z^2}$. Near the cyclotron frequency ω_c where $\eta \rightarrow 1$ we have

$$\omega = \sqrt{\frac{\omega_c q_y \sigma_H (q_z + iq_x)}{\epsilon_0 \epsilon q^2} + \omega_c^2}. \quad (8)$$

Because the Fermi level is on the Weyl nodes, we have $\sigma_{ii} = \frac{iD_0}{\omega} \approx 0$ which has little effect on the plasmon frequency.

From the microscopic Ohm's law we have $\mathbf{j} = -i\hat{\sigma}\mathbf{q}\phi$, then the unit vector of the current density is

$$\mathbf{j}_e = \frac{1}{\mathcal{N}} \begin{pmatrix} \frac{iD_0 q_x \omega - q_y \sigma_H \omega^2 - D_0 q_z \omega_c}{\omega^2 - \omega_c^2} \\ q_x \sigma_H + iD_0 q_y / \omega \\ \frac{iD_0 q_z \omega + D_0 q_x \omega_c + i q_y \sigma_H \omega \omega_c}{\omega^2 - \omega_c^2} \end{pmatrix}, \quad (9)$$

where \mathcal{N} is the normalization coefficient. The functional form of the current density is universal and independent on the details of the plasmon dispersion. The Berry curvature of the plasmon is defined by [75,78]

$$\mathbf{\Omega}(\mathbf{q}) = -i\nabla_{\mathbf{q}} \times \langle \mathbf{j}_e | \nabla_{\mathbf{q}} | \mathbf{j}_e \rangle. \quad (10)$$

The Chern number of a plane in the reciprocal space reads as a integral that $C_{\alpha\beta}(q_\gamma) = \frac{1}{2\pi} \int dS_{\alpha\beta} \cdot \mathbf{\Omega}(q_\alpha, q_\beta, q_\gamma)$. When $\omega_c = 0$ or $\sigma_H = 0$ or $D_0 = 0$, we have $\mathbf{\Omega}(\mathbf{q}) = 0$. It is a trivial phase. But when $D_0 \sigma_H \omega_c \neq 0$ and $D_0 \rightarrow 0$, $\mathbf{\Omega}(\mathbf{q})$ is diverging near $\mathbf{q} = 0$. As a result, there emerges nonzero Chern numbers $C_{zx} = -1 (C_{xy} = 1)$ for a fixed $q_y = q_0 (q_z = q_0)$ where q_0 is an arbitrary nonzero real number. When there is a section of the body, the corresponding topologically protected surface states emerge. Just as shown in Fig. 1(b), one could clearly see that the nontrivial geometric phase of the bulk plasmon is in consistent with the one-way propagation of the surface plasmons. On the other hand, C_{yz} is always zero and accordingly there are no unidirectional plasmons on the z (y) direction of the top (front) surface, seen in Fig. 6 in Appendix D.

V. SEMICLASSICAL PICTURE FOR WEYL ORBITS

Before further discussions, let us turn our attention to the electron transport for a moment. In the presence of a uniform moderate magnetic field $\mathbf{B} = (0, B, 0)$, we use a semiclassical formalism with the effect of Berry phase taken into account

[79]. Also for typical Weyl semimetals, the Zeeman splitting is small for moderate magnetic field [23]. In our case it is in the order of sub-meV (one order of magnitude smaller than the typical energy scale considered in this paper), thus it could be neglected. The equations of motion for an electron wave packet in the Fermi arcs are

$$\dot{\mathbf{r}} = \frac{\partial E_{\mathbf{k}}}{\hbar \partial \mathbf{k}} - \dot{\mathbf{k}} \times \boldsymbol{\Omega}^{\text{arc}}(\mathbf{k}), \quad (11)$$

$$\hbar \dot{\mathbf{k}} = -e\dot{\mathbf{r}} \times \mathbf{B}, \quad (12)$$

where $\boldsymbol{\Omega}^{\text{arc}}(\mathbf{k}) = (\Omega_{yz}, \Omega_{zx}, \Omega_{xy})$ is the pseudovector of the Fermi-arc Berry curvature. Different from the traditional 2D electron gas, the electrons in Fermi arcs not only float on the surface, but also penetrate deep into the interior, forming a special 3D charge distribution. By replacing k_y with $-i\partial_y$, we calculate the Fermi-arc Berry curvature $\boldsymbol{\Omega}^{\text{arc}}(\mathbf{k})$ and find that $\Omega_{zx} = 0$, $\Omega_{xy}(\lambda k_z, \lambda' k_x) = \Omega_{xy}(k_z, k_x)$, $\Omega_{yz}(\lambda k_z, \lambda' k_x) = \lambda \lambda' \Omega_{yz}(k_z, k_x)$ where $\lambda, \lambda' = \pm 1$ (see Appendix E). Combining Eqs. (11) and (12), one can see that the Fermi-arc electrons earn an anomalous velocity component perpendicular to the surface:

$$v_{\perp} = \frac{eB}{\hbar} (v_z \Omega_{xy} + v_x \Omega_{yz}). \quad (13)$$

In Fig. 2(b) we plot the variation curves of Ω_{yz} and Ω_{xy} along the top-surface Fermi arc. It indicates that near the Weyl nodes, the Berry curvature earns a sharp peak. So the electrons near Weyl nodes suffer the biggest impact and gain largest tunneling velocity, which is one order of magnitude bigger than the intrinsic speed. Suppose the magnetic field intensity B is 1 T, the relaxation time of electrons is 1 ps, the tunneling distance can reach 1 μm , which could even be enhanced linearly by B . Such a long mean free path can allow electrons to tunnel between the opposite surfaces without scattering [44,45].

As $v_z(\lambda k_z, \lambda' k_x) = \lambda v_z(k_z, k_x)$ and $v_x(\lambda k_z, \lambda' k_x) = \lambda' v_x(k_z, k_x)$, the anomalous velocity obeys $v_{\perp}(\lambda k_z, \lambda' k_x) = \lambda v_{\perp}(k_z, k_x)$. Thus, the electron earns opposite motions near different Weyl nodes, resulting a complete cyclotron motion through the Weyl semimetal, as shown in Fig. 2(a). From a quantum view, these Weyl orbits are composed of Fermi arcs on the surface and chiral zeroth LLs in the bulk [41–43]. They are unique 3D electron states connecting the opposite surfaces. When the density of electrons in the orbits is fluctuated by external field, there will be corresponding collective excitations mixing the surface plasmons and the chiral bulk plasmons [66,67].

VI. TOPOLOGICAL FERMI-ARC PLASMONS

As a result of the formation of Weyl orbits, the Fermi-arc plasmons over opposite surfaces can make up a unique 3D topological plasmon. We first focus our attention on the top surface where $y = 0$ and $q_x > 0$. From the microscopic Ohm's law we have $\mathbf{j}^s = -i\sigma^s \mathbf{q}\phi|_{0-}$, then the unit vector of the surface current density is

$$\mathbf{j}_e^s = \frac{1}{\mathcal{N}_s} \begin{pmatrix} \gamma q_z - i\eta q_x \\ q_x + i\gamma \eta q_z \end{pmatrix}, \quad (14)$$

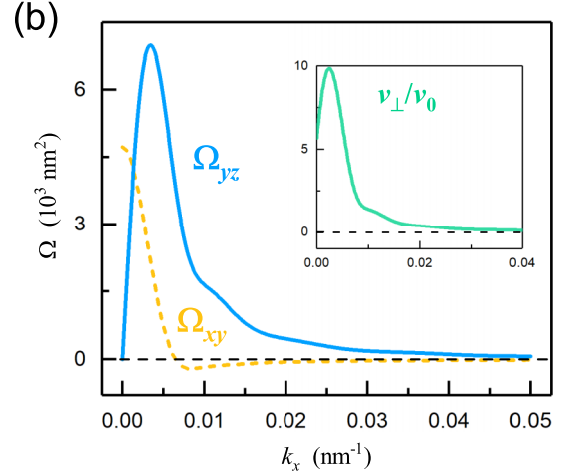
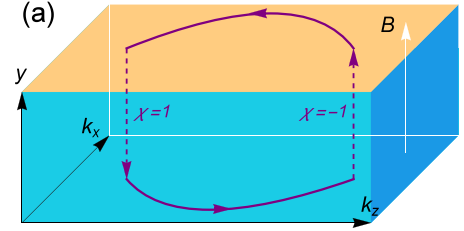


FIG. 2. (a) A schematic diagram of the Weyl orbits in a slab of Weyl semimetal with thickness L . (b) Variation curves of the Berry curvature Ω_{xy} and Ω_{yz} along the top-surface Fermi arc for $k_z, k_x > 0$. The right inset shows the corresponding anomalous velocity perpendicular to the surface. $v_0 = \sqrt{v_z^2 + v_x^2}$. $A = 0.5$ eV nm, $M = 5$ eV nm², $D_1 = 2$ eV nm², $D_2 = 3$ eV nm², $b = 0.3$ nm⁻¹, $L = 100$ nm, $B = 1$ T.

where $\mathcal{N}_s = \sqrt{(1 + \eta^2)(q_x^2 + \gamma^2 q_z^2)}$ is the normalization coefficient and $\gamma = \frac{\sigma_{zz}^s}{\sigma_{xx}^s} = \frac{D_z}{D_x}$. The functional form of Eq. (14) is universal and not dependent on the details of the plasmon dispersion. We define the pseudospin of the current density as $\mathbf{s} = \langle \mathbf{j}_e^s | \boldsymbol{\sigma}^s | \mathbf{j}_e^s \rangle$:

$$s_y = -\sin \theta, \quad s_z = \cos \theta \cos \phi, \quad s_x = \cos \theta \sin \phi, \quad (15)$$

where $\tan \theta/2 = \eta$, $\tan \phi/2 = \gamma q_z/q_x$. Because $\eta \in [0, 1]$, $\gamma q_z/q_x \in (-\infty, +\infty)$, one can see that θ changes from zero to $\pi/2$ and ϕ from $-\pi$ to π . When $\omega_c = 0$, $s_y = 0$, Eq. (15) describes a circle in the s_z - s_x plane and there is no curvature in it. But when $\omega_c > 0$, $s_y < 0$, the pseudospin \mathbf{s} will distribute on a semisphere exhibiting a curved pseudospin texture. As a result, there emerges a nonzero geometric phase in the Fermi-arc plasmons.

The electrodynamic equations can be transformed into an equivalent Hamiltonian eigenvalue problem $\omega \mathbf{j}^s = H \mathbf{j}^s$ where (see Appendix B 7)

$$H = \frac{\boldsymbol{\sigma}^s}{i[(\epsilon + 1)\epsilon_0 q - \sigma_H q_x / \omega]} \begin{pmatrix} q_z^2 & q_z q_x \\ q_x q_z & q_x^2 \end{pmatrix}. \quad (16)$$

One can find that the eigenvector of the Hamiltonian is exactly Eq. (14). When $\sigma_H = 0$, Eq. (16) describes the traditional 2DEG magnetoplasmon problem [75,78]. When $q_x > 0$ for

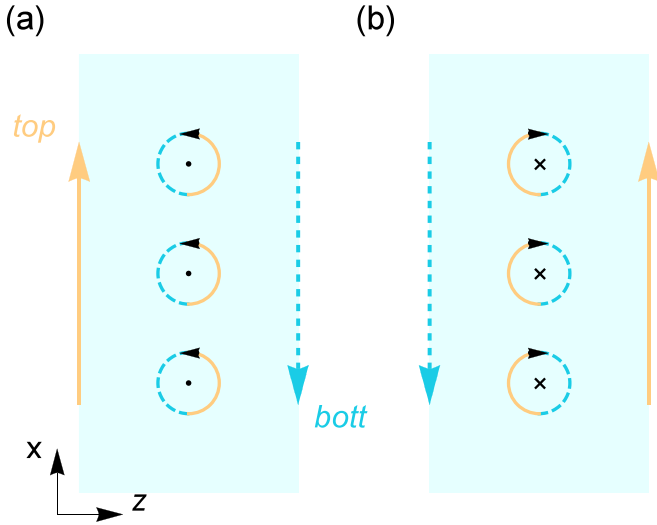


FIG. 3. Diagrammatic top view of the direction and position of the unidirectional edge plasmons with different magnetic fields. The circles with arrows denote the cyclotron motion of the Fermi-arc electrons.

the top surface, straightforward derivation implies the Chern number C_{top} of the hyperbolic band is $\frac{1}{2}$ (see Appendix B 6). Likewise, for the bottom we have $C_{\text{bottom}} = \frac{1}{2}$. Therefore, there is a nontrivial 3D topological hyperbolic plasmon with Chern number $C = 1$ over the opposite Fermi arcs.

VII. UNIDIRECTIONAL EDGE PLASMONS

Now we come to consider the edge states of the topological Fermi-arc plasmons. Near the left edge as plotted in Fig. 3(a), we assume that the electric potential of the edge plasmons takes a form as $\phi(z, x) = \phi_0 e^{-k_z z + i q_x x}$ where $k_z > 0$, $z > 0$. Compared with the surface plasmons where $\phi \propto e^{i q_z z + i q_x x}$, the edge plasmon can be described with Eq. (14) by replacing q_z with $i k_z$. From the boundary condition $J_z^{\text{edge}}|_{0^+} = 0$, we obtain $k_z = \frac{\eta q_x}{\gamma}$. Because $\eta, \gamma > 0$, one can find that $q_x > 0$ and so the edge plasmon is unidirectional propagating along the positive x axis. On the contrary, for the right edge the edge plasmon goes along the negative direction.

When the external magnetic field is along the negative direction of the y axis, as plotted in Fig. 3(b), the cyclotron motion of the Fermi-arc electrons will turn around and η becomes negative. Accordingly, the top edge plasmon would propagate along the right boundary and the bottom along the left. Therefore, the direction and position of the unidirectional edge plasmons can be adjusted by the external magnetic field, which is one distinguished feature of magnetoplasmons different from that of the usual plasmons considered in [48,56,57].

In the low frequency range $\omega \ll \alpha \tilde{\sigma}_H$, combining Eqs. (14) and (16), one can get the frequency of the edge plasmons:

$$\omega_{\text{edge}} = \left(v - \frac{D_x}{\tilde{\sigma}_H} \right) q_x, \quad (17)$$

which implies a gapless linear edge mode independent of the external magnetic field.

VIII. CONCLUSION

In summary, we have systematically investigated the properties of bulk, surface, and edge plasmons in Weyl semimetals in the presence of a magnetic field. It is found that unidirectional plasmons with different properties exist on different surfaces, which is consistent with the nontrivial topology of the 3D bulk plasmons. These novel plasmons possess momentum-location lock and are mixed with the bulk LL plasmons. The anomalous Hall conductivity can greatly change the magnetoplasmon dispersion and gives rise to linear, parabolic, or even hyperbolic bands, measurable by EELS [50,57]. Strong confinement of the EM field associated with Fermi-arc plasmons has been found. With the help of a semi-classical picture for the formation of the Weyl orbits, we point out that the Fermi-arc plasmons at opposite surfaces can make up another unique 3D topological plasmon. Furthermore, there is a gapless unidirectional edge plasmon protected by the topology whose direction and position can be controlled by an external field. Our work thus uncovers topological features of Weyl plasmons, which may have important applications in photoelectric devices based on chiral/topological plasmonics.

ACKNOWLEDGMENTS

This work was supported by National Key Research and Development Program of China (Grant No. 2017YFA0303400), NSFC-RGC (Grant No. 11861161002), National Natural Science Foundation of China (Grants No. 11774036 and No. 12174032), and China Postdoctoral Science Foundation (Grant No. 2019M650583).

APPENDIX A: THE EFFECT OF MAGNETIC FIELD ON THE CONDUCTIVITY

In the presence of a uniform magnetic field $\mathbf{B} = (0, B, 0)$, the equation of motion for an electron reads

$$\frac{\partial \mathbf{j}}{\partial t} = \frac{e^2 n}{m} \mathbf{E} + \omega_c \mathbf{e}_y \times \mathbf{j}, \quad (A1)$$

$$\begin{pmatrix} 1 & 0 & -i\eta \\ 0 & 1 & 0 \\ i\eta & 0 & 1 \end{pmatrix} \mathbf{j} = \hat{\sigma} \mathbf{E}, \quad (A2)$$

where $e > 0$, $\eta = \omega_c / \omega$ with a cyclotron frequency $\omega_c = eB/m$ from the perpendicular magnetic field and $\hat{\sigma} = i \frac{e^2 n}{m \omega}$ is the well-known 3D conductivity. In the case of Weyl semimetals, the conductivity is a matrix and Eq. (A2) becomes

$$\begin{pmatrix} 1 & 0 & -i\eta \\ 0 & 1 & 0 \\ i\eta & 0 & 1 \end{pmatrix} \mathbf{j} = \begin{pmatrix} \sigma_{xx} & -\sigma_H & 0 \\ \sigma_H & \sigma_{yy} & 0 \\ 0 & 0 & \sigma_{zz} \end{pmatrix} \mathbf{E}, \quad (A3)$$

where $\sigma_H = \frac{e^2}{2\pi h} 2b$ is the anomalous Hall conductivity. Then

$$\mathbf{j} = \begin{pmatrix} \frac{\sigma_{xx}}{1-\eta^2} & \frac{-\sigma_H}{1-\eta^2} & \frac{i\sigma_{zz}\eta}{1-\eta^2} \\ \sigma_H & \sigma_{yy} & 0 \\ \frac{-i\sigma_{xx}\eta}{1-\eta^2} & \frac{i\sigma_H\eta}{1-\eta^2} & \frac{\sigma_{zz}}{1-\eta^2} \end{pmatrix} \mathbf{E}. \quad (A4)$$

For the surface we have

$$\begin{pmatrix} j_z^s \\ j_x^s \end{pmatrix} = \begin{pmatrix} \frac{\sigma_{zz}^s}{1-\eta^2} & \frac{-i\sigma_{xz}^s\eta}{1-\eta^2} \\ \frac{i\sigma_{xz}^s\eta}{1-\eta^2} & \frac{\sigma_{xx}^s}{1-\eta^2} \end{pmatrix} \begin{pmatrix} E_z|0^- \\ E_x|0^- \end{pmatrix}. \quad (\text{A5})$$

APPENDIX B: PLASMONS ON THE TOP SURFACE

1. The wave vector perpendicular to the surface

For the top surface at $y = 0$, when $y > 0$, we assume the electric potential takes the form as $\phi(x, y > 0, z) = \phi_0 e^{-\kappa y} e^{i(q_z z + q_x x - \omega t)}$. From the Poisson equation $\nabla^2 \phi = 0$, one can get

$$\kappa = q = \sqrt{q_z^2 + q_x^2}. \quad (\text{B1})$$

When $y < 0$ we assume that $\phi(x, y < 0, z) = \phi_0 e^{\kappa y} e^{i(q_z z + q_x x - \omega t)}$, $\rho(x, y < 0, z) = \rho_0 e^{\kappa y} e^{i(q_z z + q_x x - \omega t)}$. Then the Poisson equation $\nabla^2 \phi = -\rho/\epsilon_0 \epsilon$ gives that

$$\rho_0 = \epsilon_0 \epsilon (q^2 - k^2) \phi_0. \quad (\text{B2})$$

Because the Fermi level is on the Weyl nodes, we assume that $\sigma_{xx} = \sigma_{yy} = \sigma_{zz} = 0$. From the charge conservation we get

$$\rho_0 = \frac{\eta k (q_z + i\eta q_x) \sigma_H}{i\omega (1 - \eta^2)} \phi_0. \quad (\text{B3})$$

From Eqs. (B2) and (B3) one can get Eq. (3) in the main text and

$$k = \frac{-\xi + \text{sgn}(\omega - \omega_c) \sqrt{\xi^2 + [2\epsilon_0 \epsilon \omega (1 - \eta^2) q]^2}}{2\epsilon_0 \epsilon \omega (1 - \eta^2)}, \quad (\text{B4})$$

where $\xi = (-i\eta q_z + \eta^2 q_x) \sigma_H$.

2. The surface density contribution from bulk/surface carriers

We assume that the surface density contribution from bulk carriers takes the form as $\rho^{s,M}(z, x) = \rho_0^M e^{i(q_z z + q_x x - \omega t)}$, then

$$\frac{\partial \rho^{s,M}}{\partial t} = \mathbf{e}_y \cdot \mathbf{j}|0^-, \quad (\text{B5})$$

$$\rho_0^M = \frac{q_x \sigma_H}{\omega} \phi_0. \quad (\text{B6})$$

On the other hand, the surface density contribution from surface carriers takes the form as $\rho^{s,F}(z, x) = \rho_0^F e^{i(q_z z + q_x x - \omega t)}$, then

$$\frac{\partial \rho^{s,F}}{\partial t} + \nabla_s \cdot \mathbf{j}^s = 0, \quad (\text{B7})$$

$$\rho_0^F = \frac{q_z^2 \sigma_{zz}^s + q_x^2 \sigma_{xx}^s + iq_z q_x \eta (\sigma_{zz}^s - \sigma_{xx}^s)}{i\omega (1 - \eta^2)} \phi_0. \quad (\text{B8})$$

3. The constitutive relation for the surface plasmon

At the top surface, the boundary condition reads

$$\epsilon_0 E_y|0^+ - \epsilon \epsilon_0 E_y|0^- = \rho^{s,M} + \rho^{s,F}, \quad (\text{B9})$$

$$q + \epsilon k = \frac{\alpha}{\omega} \left[q_x \tilde{\sigma}_H + \frac{q_z^2 \tilde{\sigma}_{zz}^s + q_x^2 \tilde{\sigma}_{xx}^s + iq_z q_x \eta (\tilde{\sigma}_{zz}^s - \tilde{\sigma}_{xx}^s)}{i(1 - \eta^2)} \right], \quad (\text{B10})$$

where $\alpha = \frac{e^2}{\hbar \epsilon_0}$, $\tilde{\sigma}_{ii}^s = \sigma_{ii}^s / \alpha \epsilon_0$, $\tilde{\sigma}_H = b/\pi$. If $\tilde{\sigma}_{zz}^s = \frac{iD_z}{\omega - vq_x}$, $\tilde{\sigma}_{xx}^s = \frac{iD_x}{\omega - vq_x}$ (see in Appendix B 4), then Eq. (B10) becomes

$$q + \epsilon k = \frac{\alpha}{\omega} \left[q_x \tilde{\sigma}_H + \frac{q_z^2 D_z + q_x^2 D_x + iq_z q_x \eta (D_z - D_x)}{(1 - \eta^2)(\omega - vq_x)} \right]. \quad (\text{B11})$$

4. Approximate expressions of the Fermi-arc conductivity

We start from the effective model for the Fermi arc at the top ($\tau = 1$) or bottom ($\tau = -1$) surface [Eq. (2) in the main text]:

$$h_\tau = \tau v k_x + (D_2 - D_1)(k_z^2 + k_x^2) + D_1 b^2 \approx \tau v k_x. \quad (\text{B12})$$

The velocity operators are given by

$$\hbar V_x = \frac{\partial h_\tau}{\partial k_x} = \tau v + 2(D_2 - D_1)k_x \approx \tau v, \quad (\text{B13})$$

$$\hbar V_z = \frac{\partial h_\tau}{\partial k_z} = 2(D_2 - D_1)k_z. \quad (\text{B14})$$

Because they are real numbers, not matrices, we have ($\mathbf{q} \rightarrow 0$)

$$\langle \Psi_\tau | \hbar V_x | \Psi_{\tau'} \rangle = \delta_{\tau\tau'} \hbar V_x, \quad (\text{B15})$$

$$\langle \Psi_\tau | \hbar V_z | \Psi_{\tau'} \rangle = \delta_{\tau\tau'} \hbar V_z. \quad (\text{B16})$$

So the Fermi-arc conductivity reads

$$\sigma_{ij}^\tau = \frac{e^2}{\hbar} \frac{i}{2\pi} \int d^2 \mathbf{k} \frac{(\hbar V_i)(\hbar V_j)(f_{\mathbf{k}}^\tau - f_{\mathbf{k}+\mathbf{q}}^\tau)}{(\hbar\omega + E_{\mathbf{k}}^\tau - E_{\mathbf{k}+\mathbf{q}}^\tau)(E_{\mathbf{k}+\mathbf{q}}^\tau - E_{\mathbf{k}}^\tau)}. \quad (\text{B17})$$

Because $E_{\mathbf{k}+\mathbf{q}}^\tau - E_{\mathbf{k}}^\tau \approx \tau v q_x$, we have ($\mathbf{q} \rightarrow 0$)

$$\sigma_{ij}^\tau \approx \alpha \epsilon_0 \frac{iD_{ij}}{\hbar\omega - \tau v q_x}, \quad (\text{B18})$$

where $D_{ij} = \frac{1}{2\pi} \int d^2 \mathbf{k} (\hbar V_i)(\hbar V_j) \frac{-df_{\mathbf{k}}^\tau}{dE_{\mathbf{k}}^\tau}$.

5. Dispersion behavior in the long wave limit

When $q_z = 0$ and $q_x \rightarrow 0$, from Eq. (3) in the main text and Eq. (B11) we have

$$\epsilon k = \frac{\alpha}{\omega} \frac{q_x \tilde{\sigma}_H \eta^2}{\eta^2 - 1} \quad (\text{B19})$$

and

$$\epsilon k = \frac{\alpha}{\omega} \left[q_x \tilde{\sigma}_H + \frac{q_x^2 D_x}{(1 - \eta^2)(\omega - vq_x)} \right]. \quad (\text{B20})$$

Then

$$\frac{q_x \tilde{\sigma}_H \eta^2}{\eta^2 - 1} = q_x \tilde{\sigma}_H + \frac{q_x^2 D_x}{(1 - \eta^2)(\omega - vq_x)}, \quad (\text{B21})$$

$$\omega = (v - D_x/\tilde{\sigma}_H) q_x. \quad (\text{B22})$$

While in the strong magnetic field limit $\omega_c \rightarrow +\infty$, from Eq. (3) in the main text and Eq. (B11) we have

$$\epsilon k = \frac{\epsilon q_x^2}{k} + \frac{\alpha q_x \tilde{\sigma}_H}{\omega} \quad (\text{B23})$$

and

$$q_x + \epsilon k = \frac{\alpha}{\omega} \left[q_x \tilde{\sigma}_H + \frac{q_x^2 D_x}{\eta^2 (v q_x - \omega)} \right]. \quad (\text{B24})$$

Then

$$q_x + \frac{\epsilon q_x^2}{k} + \frac{\alpha q_x \tilde{\sigma}_H}{\omega} = \frac{\alpha}{\omega} \left[q_x \tilde{\sigma}_H + \frac{q_x^2 D_x}{\eta^2 (v q_x - \omega)} \right], \quad (\text{B25})$$

$$1 + \frac{\epsilon q_x}{k} = \frac{\alpha}{\omega} \frac{q_x D_x}{\eta^2 (v q_x - \omega)}. \quad (\text{B26})$$

In the long wave limit $q_x \rightarrow 0$ one gets

$$1 = \frac{\alpha}{\omega} \frac{q_x D_x}{\eta^2 (v q_x - \omega)}. \quad (\text{B27})$$

Because $q_x/\eta^2 \rightarrow 0$, in order to make the equation satisfied one has $(v q_x - \omega) \rightarrow 0$. Thus

$$\omega = v q_x. \quad (\text{B28})$$

6. Topological plasmon in a hyperbolic band

From Eq. (A5) we have

$$\begin{pmatrix} j_z^s \\ j_x^s \end{pmatrix} = \begin{pmatrix} \frac{\sigma_{zz}^s}{1-\eta^2} & \frac{-i\sigma_{xz}^s \eta}{1-\eta^2} \\ \frac{i\sigma_{xz}^s \eta}{1-\eta^2} & \frac{\sigma_{xx}^s}{1-\eta^2} \end{pmatrix} \begin{pmatrix} -iq_z \\ -iq_x \end{pmatrix} \phi|_{0^-}. \quad (\text{B29})$$

Then the unit vector of the current is

$$\mathbf{j}_e^s = \frac{1}{\sqrt{\frac{\omega^2 + \omega_c^2}{\omega^2} (q_x^2 + \gamma^2 q_z^2)}} \begin{pmatrix} \gamma q_z - i \frac{\omega_c}{\omega} q_x \\ q_x + i \gamma \frac{\omega_c}{\omega} q_z \end{pmatrix}, \quad (\text{B30})$$

where $\gamma = \frac{\sigma_{zz}^s}{\sigma_{xx}^s} = \frac{D_z}{D_x} \approx 0$.

The Berry curvature is defined by $\mathbf{\Omega} = -i \nabla_{\mathbf{q}} \times \langle \mathbf{j}_e^s | \nabla_{\mathbf{q}} | \mathbf{j}_e^s \rangle$, and direct derivation shows that

$$\mathbf{\Omega} = \left(0, \frac{2\gamma \omega_c (\omega^2 - \omega_c^2) (q_z \partial_z \omega + q_x \partial_x \omega)}{(q_x^2 + \gamma^2 q_z^2) (\omega^2 + \omega_c^2)^2}, 0 \right). \quad (\text{B31})$$

Because $\partial_z \omega \approx 0$, we make

$$\Omega^y = \frac{2\gamma \omega_c (\omega^2 - \omega_c^2) q_x d_x \omega}{(q_x^2 + \gamma^2 q_z^2) (\omega^2 + \omega_c^2)^2}, \quad (\text{B32})$$

which does not change the topology of the band. Then

$$\frac{1}{2\pi} \int_{-\infty}^{+\infty} \Omega^y d q_z = \frac{q_x}{|q_x|} \frac{\omega_c (\omega^2 - \omega_c^2) d_x \omega}{(\omega^2 + \omega_c^2)^2}. \quad (\text{B33})$$

The Chern number is $C = \frac{1}{2\pi} \int \mathbf{\Omega} \cdot d\mathbf{S}_{\mathbf{q}}$ which can be decomposed into two parts that $C = C_{\uparrow} + C_{\downarrow}$ where C_{\uparrow} is for the upper half-band $\omega_{\uparrow} \in [\omega_m, +\infty]$ and C_{\downarrow} is for the lower half-band $\omega_{\downarrow} \in [\omega_c, \omega_m]$. For the lower half-band ω_{\downarrow} , we choose $d\mathbf{S}_{\mathbf{q}} = -d q_z d q_x$ possessing an opposite direction to the upper half. When $q_x > 0$, we have

$$C_{\uparrow} = \int_{\omega_m}^{+\infty} \frac{\omega_c (\omega_{\uparrow}^2 - \omega_c^2)}{(\omega_{\uparrow}^2 + \omega_c^2)^2} d\omega_{\uparrow} \quad (\text{B34})$$

and

$$C_{\downarrow} = - \int_{\omega_m}^{\omega_c} \frac{\omega_c (\omega_{\downarrow}^2 - \omega_c^2)}{(\omega_{\downarrow}^2 + \omega_c^2)^2} d\omega_{\downarrow}. \quad (\text{B35})$$

Thus

$$C_{\text{top}} = \int_{\omega_c}^{+\infty} \frac{\omega_c (\omega^2 - \omega_c^2)}{(\omega^2 + \omega_c^2)^2} d\omega = \frac{1}{2}. \quad (\text{B36})$$

When $q_x < 0$, we also have $C_{\text{bot}} = \frac{1}{2}$. Thus $C_{\text{tot}} = 1$.

7. Equivalent Hermitian eigenvalue problem

From Eq. (B5) we have

$$\rho^{s,M} = \frac{i\sigma_H E_x|_{0^-}}{\omega}. \quad (\text{B37})$$

From Eq. (B7) we have

$$-i\omega \rho^{s,F} + iq_z j_z^s + iq_x j_x^s = 0, \quad (\text{B38})$$

$$\rho^{s,F} = \frac{q_z j_z^s + q_x j_x^s}{\omega}. \quad (\text{B39})$$

So the surface density is

$$\rho^s = \frac{q_z j_z^s + q_x j_x^s}{\omega} + \frac{i\sigma_H E_x|_{0^-}}{\omega}. \quad (\text{B40})$$

The components of electric field satisfy

$$\frac{E_y|_{0^-}}{E_z|_{0^-}} = \frac{k}{iq_z} \approx \frac{q}{iq_z}, \quad (\text{B41})$$

$$E_y|_{0^-} = \frac{q}{iq_z} E_z|_{0^-}, \quad (\text{B42})$$

and

$$E_y|_{0^+} = \frac{-q}{iq_z} E_z|_{0^-}, \quad (\text{B43})$$

$$E_x|_{0^-} = \frac{q_x}{q_z} E_z|_{0^-}. \quad (\text{B44})$$

From Eq. (B9) we have

$$\epsilon_0 \frac{-q}{iq_z} E_z|_{0^-} - \epsilon \epsilon_0 \frac{q}{iq_z} E_z|_{0^-} = \frac{q_z j_z^s + q_x j_x^s}{\omega} + \frac{i\sigma_H q_x}{\omega q_z} E_z|_{0^-}, \quad (\text{B45})$$

$$E_z|_{0^-} = \frac{q_z^2 j_z^s + q_x q_x j_x^s}{i[(\epsilon + 1)\epsilon_0 \omega q - \sigma_H q_x]}. \quad (\text{B46})$$

Then

$$E_x|_{0^-} = \frac{q_x}{q_z} E_z|_{0^-} = \frac{q_z q_x j_z^s + q_x^2 j_x^s}{i[(\epsilon + 1)\epsilon_0 \omega q - \sigma_H q_x]}. \quad (\text{B47})$$

Thus

$$\begin{pmatrix} E_z|_{0^-} \\ E_x|_{0^-} \end{pmatrix} = \frac{1}{i[(\epsilon + 1)\epsilon_0 \omega q - \sigma_H q_x]} \begin{pmatrix} q_z^2 & q_z q_x \\ q_z q_x & q_x^2 \end{pmatrix} \begin{pmatrix} j_z^s \\ j_x^s \end{pmatrix}. \quad (\text{B48})$$

Combining Eq. (A5) one can obtain

$$\omega \begin{pmatrix} j_z^s \\ j_x^s \end{pmatrix} = H \begin{pmatrix} j_z^s \\ j_x^s \end{pmatrix}, \quad (\text{B49})$$

where

$$H = \frac{1}{i[(\epsilon + 1)\epsilon_0 \omega q - \sigma_H q_x / \omega]} \begin{pmatrix} \frac{\sigma_{zz}^s}{1-\eta^2} & \frac{-i\sigma_{xz}^s \eta}{1-\eta^2} \\ \frac{i\sigma_{xz}^s \eta}{1-\eta^2} & \frac{\sigma_{xx}^s}{1-\eta^2} \end{pmatrix} \begin{pmatrix} q_z^2 & q_z q_x \\ q_z q_x & q_x^2 \end{pmatrix}. \quad (\text{B50})$$

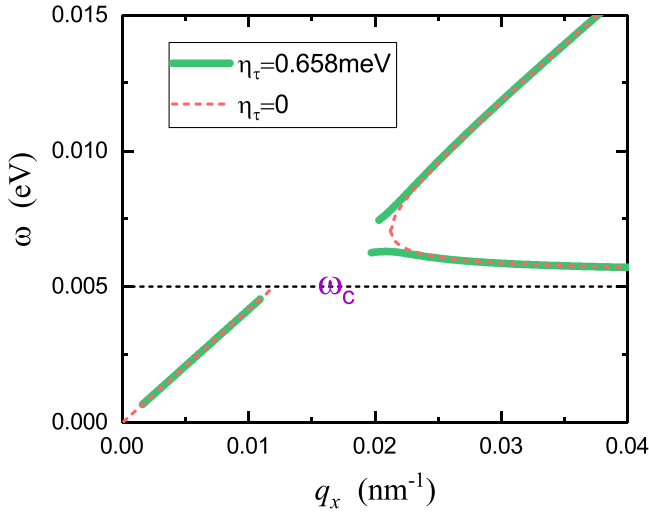


FIG. 4. The influence of relaxation time from scattering. $\eta_\tau = 0.658$ meV. The other parameters are the same as Fig. 1(a) in the main text.

8. The influence of relaxation time from scattering

When considering the effects of defects and impurities in realistic systems, a relaxation time term is added to the conductivity [62]. Here we choose $\tilde{\sigma}_{zz}^s = \frac{iD_z}{\omega + i\eta_\tau - vq_x}$, $\tilde{\sigma}_{xx}^s = \frac{iD_x}{\omega + i\eta_\tau - vq_x}$, where $\eta_\tau = \hbar/\tau = 0.658$ meV and $\tau = 1$ ps. As a result, the wave vector k and the frequency ω of the plasmons obtain a imaginary part, and the plasmon lifetime becomes finite by damping. Under the conditions $\text{abs}[\text{Re}(k)] > \text{abs}[\text{Im}(k)]$ and $\text{abs}[\text{Re}(\omega)] > \text{abs}[\text{Im}(\omega)]$, one may have a well-defined (long-lived) plasmon. The energy scale related to scattering η_τ is in the order of sub-meV, which is one order of magnitude smaller than the typical energy scale of plasmons. Thus, one can expect that the basic physical picture remains unchanged.

Perturbative calculation shows that the dispersion relationship in the z direction (with $q_x = 0$) has the form $\omega = \sqrt{\alpha D_z |q_z| + \omega_c^2 (1 - i\delta)}$, with $\delta = \eta_\tau \alpha D_z |q_z| / 2(\alpha D_z |q_z| + \omega_c^2)^{3/2}$. It is estimated that $\delta < 0.033$ (for $\omega_c = 5$ meV). The scattering leads to minor correction to the dispersion relation with finite lifetime of plasmon. We display the dispersion relationship in the x direction (with $q_z = 0$) in Fig. 4 with the constraints $\text{abs}[\text{Re}(k)] > \text{abs}[\text{Im}(k)]$ and $\text{abs}[\text{Re}(\omega)] > \text{abs}[\text{Im}(\omega)]$. From Fig. 4 we can see that the linear branch and the hyperbolic branch keep the shape stable, except for a small split of the the latter. The plasmon modes between the gap are not plotted because their lifetimes are short by damping. For the frequencies ω far from ω_c , which contribute the most to the Berry curvature of the band, the influence of relaxation time is even smaller. Thus the scattering from defects/impurities leads to finite lifetime of plasmons, and the dispersion relations of the plasmons are robust against scattering effect.

APPENDIX C: PLASMONS ON THE RIGHT SURFACE

When considering the right surface, we assume the electric potential near the surface ($x = 0$) takes the form

as $\phi(x > 0, y, z) = \phi_0 e^{-\kappa x} e^{i(q_y y + q_z z - \omega t)}$, $\phi(x < 0, y, z) = \phi_0 e^{\kappa x} e^{i(q_y y + q_z z - \omega t)}$. Accordingly, Eq. (3) in the main text becomes

$$\epsilon_0 \epsilon (q^2 - k^2) = \frac{\eta q_y (q_z + \eta k) \sigma_H}{(1 - \eta^2) \omega}. \quad (\text{C1})$$

Like in the top case, there is also topological Fermi arc on the right surface. The boundary condition gives the constitutive relation of the surface plasmons that

$$q + \epsilon k = \frac{\alpha}{\omega} \left[\frac{-q_y \tilde{\sigma}_H}{1 - \eta^2} + \frac{q_y^2 D_y + q_z^2 D_z / (1 - \eta^2)}{\omega + v q_y} \right]. \quad (\text{C2})$$

Hence the magnetic field has different influence on the arc electrons in different directions. This is because the vertical magnetic field is parallel to the right surface.

1. On the y direction

When $q_z = 0$, Eq. (C2) becomes

$$|q_y| + \epsilon k = \frac{\alpha}{\omega} \left[\frac{-q_y \tilde{\sigma}_H}{1 - \eta^2} + \frac{q_y^2 D_y}{\omega + v q_y} \right]. \quad (\text{C3})$$

Numerical calculation suggests that $q_y < 0$, so the surface plasmon propagates along the negative y direction. This is a result of the negative sign in $-q_y \tilde{\sigma}_H / (1 - \eta^2)$ in Eq. (C3). In the long wave limit $q_y \rightarrow 0$ and $\omega \rightarrow 0$, Eqs. (C1) and (C3) become

$$k = -q_y \frac{\epsilon \omega}{\alpha \tilde{\sigma}_H} \rightarrow 0 \quad (\text{C4})$$

and

$$\omega = \sqrt[3]{\frac{-q_y D_y \omega_c^2}{\tilde{\sigma}_H}}, \quad (\text{C5})$$

proposing a gapless surface plasmon with a novel dispersion $\omega \propto \sqrt[3]{q_y}$ as plotted in Fig. 5.

In the limit that $\omega = \omega_c - \tau$ where $\tau \rightarrow 0^+$, we have $\eta \rightarrow 1$. Equations (C4) and (C5) change into

$$k = -q_y \frac{\epsilon \omega_c (\eta^2 - 1)}{\alpha \tilde{\sigma}_H} \rightarrow 0 \quad (\text{C6})$$

and

$$\omega = -v q_y, \quad (\text{C7})$$

which gives a linear surface mode.

In the limit that $\omega = \omega_c + \tau$ where $\tau \rightarrow 0^+$, Eq. (C6) becomes

$$k = -q_y \frac{\alpha \tilde{\sigma}_H}{\epsilon \omega_c (1 - \eta^2)} \rightarrow +\infty. \quad (\text{C8})$$

From Eq. (C1) we have

$$\epsilon k = \frac{\alpha q_y \tilde{\sigma}_H \eta^2}{\omega (\eta^2 - 1)}. \quad (\text{C9})$$

From Eq. (C3) we have

$$\epsilon k = \frac{\alpha}{\omega} \left[\frac{q_y \tilde{\sigma}_H}{\eta^2 - 1} + \frac{q_y^2 D_y}{\omega + v q_y} \right]. \quad (\text{C10})$$

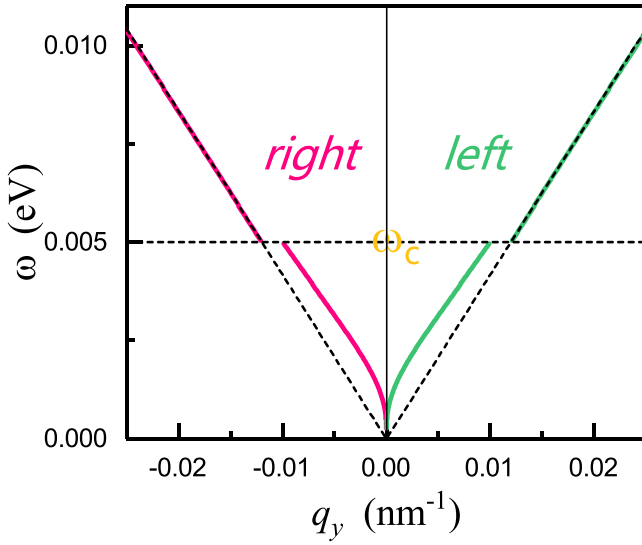


FIG. 5. Dispersion of Weyl surface plasmons on the left and right surfaces. $D_x = 0.05$ eV, $q_z = 0$, $\hbar\omega_c = 5$ meV, $v = 0.5$ eV nm, $\tilde{\sigma}_H = 0.6$. The dashed lines denote the dispersions that $\omega = \pm(v - D_x/\tilde{\sigma}_H)q_x$ and $\omega = \omega_c$.

Then

$$\frac{q_y \tilde{\sigma}_H \eta^2}{\eta^2 - 1} = \frac{q_y \tilde{\sigma}_H}{\eta^2 - 1} + \frac{q_y^2 D_y}{\omega + v q_y}, \quad (\text{C11})$$

$$\omega = -(v - D_y/\tilde{\sigma}_H)q_y. \quad (\text{C12})$$

Thus there is a gap in the wave vector near $\omega \approx \omega_c$:

$$\Delta q_y = \frac{\omega_c}{v - D_y/\tilde{\sigma}_H} - \frac{\omega_c}{v}. \quad (\text{C13})$$

2. On the z direction

When $q_y = 0$, from Eq. (C1) we have $k = |q_z|$, then Eq. (C2) becomes

$$(1 + \epsilon)\omega^2 = \alpha \frac{D_z |q_z|}{1 - \eta^2}, \quad (\text{C14})$$

$$\omega = \sqrt{\omega_c^2 + \frac{\alpha D_z |q_z|}{1 + \epsilon}}, \quad (\text{C15})$$

which is a traditional magnetoplasmon dispersion and it can travel in both directions. This plasmon originates from electronic oscillations of the surface Fermi arcs.

When $D_z = 0$, $q_y \rightarrow 0$ but $q_y \neq 0$, we seek for solutions near $\omega \approx \omega_c$ ($\eta \approx 1$). From Eq. (C1) we have

$$\epsilon(q_z^2 - k^2)\omega = \frac{\alpha \eta q_y (q_z + \eta k) \tilde{\sigma}_H}{1 - \eta^2}. \quad (\text{C16})$$

From Eq. (C2) we have

$$(|q_z| + \epsilon k)\omega = \frac{\alpha q_y \tilde{\sigma}_H}{\eta^2 - 1}. \quad (\text{C17})$$

Then

$$\frac{\epsilon(k^2 - q_z^2)}{|q_z| + \epsilon k} = q_z + k, \quad (\text{C18})$$

$$q_z = -k < 0. \quad (\text{C19})$$

So there is a surface plasmon propagating along the negative z direction and $\omega \approx \omega_c$. This is a robust result of the product factor $(q_z + \eta k)$ in Eq. (C1). Furthermore, when $D_z \rightarrow 0$ with a large $q_y > 0$, this unidirectional plasmon can still exist, which cannot be excited from the surface Fermi arcs requiring $q_y < 0$. Thus it originates from the topology of the bulk plasmon where $C_{zx} = -1$.

APPENDIX D: PLASMONS ON THE FRONT SURFACE

Now we turn to the front surface and assume the electric potential near the surface ($z = 0$) takes the form as $\phi(x, y, z > 0) = \phi_0 e^{-kz} e^{i(q_x x + q_y y - \omega t)}$, $\phi(x, y, z < 0) = \phi_0 e^{kz} e^{i(q_x x + q_y y - \omega t)}$. Accordingly, Eq. (3) in the main text becomes

$$\epsilon_0 \epsilon (q^2 - k^2) = \frac{i \eta q_y (\eta q_x - k) \sigma_H}{(1 - \eta^2) \omega}. \quad (\text{D1})$$

Because there is no electron states on the x - y surface, the constitutive relation of the surface plasmons is constituted only of the anomalous Hall conductivity:

$$(q + \epsilon k)\omega(1 - \eta^2) = \alpha i \eta q_y \tilde{\sigma}_H. \quad (\text{D2})$$

When $q_y = 0$, Eq. (D1) reads $k = |q_x|$ and Eq. (D2) gives

$$|q_x|(1 + \epsilon)\omega(1 - \omega_c^2/\omega^2) = 0, \quad (\text{D3})$$

$$\omega = \omega_c. \quad (\text{D4})$$

This surface plasmon is completely induced by the magnetic field, very different from the traditional magnetoplasmons which vanish in the insulated phase.

From Eqs. (D1) and (D2) one can get

$$\frac{\epsilon(q^2 - k^2)}{q + \epsilon k} = \eta q_x - k. \quad (\text{D5})$$

When $q_y \rightarrow 0$, from Eq. (D1) we have $k = q_x$ and then Eq. (D3) becomes

$$0 = |q_x|(\text{sgn}(q_x) - 1). \quad (\text{D6})$$

Thus $q_x > 0$ and the surface plasmon propagates along the positive x direction. This is a robust result of the product factor $(\eta q_x - k)$ in Eq. (D1).

When $q_x = 0$, from Eq. (D5) we have

$$\epsilon(q_y^2 - k^2) = -k(|q_y| + \epsilon k), \quad (\text{D7})$$

$$k = -\epsilon |q_y| < 0, \quad (\text{D8})$$

which conflicts with the original assumption. So there is no surface plasmon propagating along the y direction. This is also consistent with the topology of the bulk plasmons, as plotted in Fig. 6.

APPENDIX E: THE BERRY CURVATURE IN FERMI ARCS AT ZERO MAGNETIC FIELD

As Eq. (1) in the main text shows, the 3D model of Weyl semimetal is

$$H = A(k_x \sigma_x + k_y \sigma_y) + M(b^2 - k^2) \sigma_z + D_1 k_y^2 + D_2 k_{\parallel}^2, \quad (\text{E1})$$

where $k_{\parallel}^2 = k_x^2 + k_z^2$. The model hosts two Weyl nodes at $(0, 0, \pm b)$ having energy $E_{\text{nodes}} = D_2 b^2$.

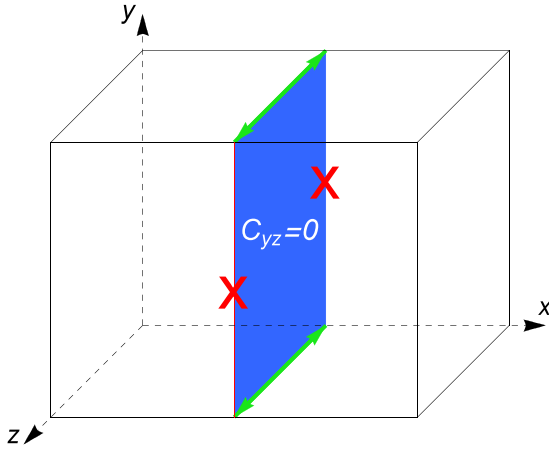


FIG. 6. Schematic diagrams of the propagation of the surface plasmons and the corresponding bulk topology.

The velocity operators are

$$\hbar V_x = \frac{\partial H}{\partial k_x} = 2(D_2 - M\sigma_z)k_x + A\sigma_x, \quad (\text{E2})$$

$$\hbar V_y = \frac{\partial H}{\partial k_y} = 2(D_1 - M\sigma_z)k_y + A\sigma_y, \quad (\text{E3})$$

$$\hbar V_z = \frac{\partial H}{\partial k_z} = 2(D_2 - M\sigma_z)k_z. \quad (\text{E4})$$

We assume the wave functions take the form that

$$\Psi_i(y) = \sum_{m=1}^{\infty} \begin{pmatrix} C_{i,1m} \\ C_{i,2m} \end{pmatrix} \varphi_m(y), \quad \Psi_j(y) = \sum_{n=1}^{\infty} \begin{pmatrix} C_{j,1n} \\ C_{j,2n} \end{pmatrix} \varphi_n(y), \quad (\text{E5})$$

where $\varphi_m(y) = \sqrt{\frac{2}{L}} \sin[\frac{m\pi}{L}(y + L/2)]$ satisfying $\int_{-L/2}^{L/2} \varphi_m(y)\varphi_n(y)dy = \delta_{mn}$. i and j are band indexes. $C_{i,1m}$ and $C_{i,2m}$ are the superposition coefficients. By replacing k_y with $-i\partial_y$, from Eqs. (E2)–(E5) we obtain that

$$\begin{aligned} \langle \Psi_i(y) | \hbar V_x | \Psi_j(y) \rangle &= \sum_n C_{i,1n}^* C_{j,1n} 2k_x (D_2 - M) \\ &+ C_{i,2n}^* C_{j,2n} 2k_x (D_2 + M) \\ &+ (C_{i,1n}^* C_{j,2n} + C_{i,2n}^* C_{j,1n}) A. \end{aligned} \quad (\text{E6})$$

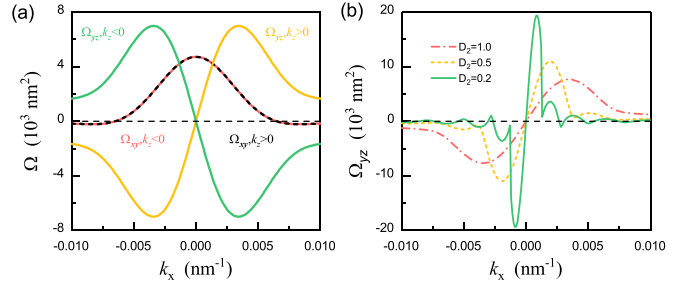


FIG. 7. (a) Variation curves of the Berry curvature Ω_{xy} and Ω_{yz} along the Fermi arcs. (b) The influence of D_2 on the Berry curvature Ω_{yz} when $D_1 = 0$. $D_2 = 1.0, 0.5$, and 0.2 eV nm², respectively.

When $m \neq n$ we have

$$\begin{aligned} &\langle \Psi_i(y) | \hbar V_y | \Psi_j(y) \rangle \\ &= i \sum_{mn} [C_{i,1m}^* C_{j,1n} (D_1 - M) \\ &+ C_{i,2m}^* C_{j,2n} (D_1 + M)] \frac{4mn[(-1)^{m+n} - 1]}{L(m^2 - n^2)}, \end{aligned} \quad (\text{E7})$$

else

$$\langle \Psi_i(y) | \hbar V_y | \Psi_j(y) \rangle = i \sum_n (C_{i,2n}^* C_{j,1n} - C_{i,1n}^* C_{j,2n}) A, \quad (\text{E8})$$

$$\begin{aligned} \langle \Psi_i(y) | \hbar V_z | \Psi_j(y) \rangle &= \sum_n C_{i,1n}^* C_{j,1n} 2k_z (D_2 - M) \\ &+ C_{i,2n}^* C_{j,2n} 2k_z (D_2 + M). \end{aligned} \quad (\text{E9})$$

Then one can get

$$\langle \Psi_i(y) | \hbar V_x | \Psi_j(y) \rangle = \langle \Psi_j(y) | \hbar V_x | \Psi_i(y) \rangle^*, \quad (\text{E10})$$

$$\langle \Psi_i(y) | \hbar V_y | \Psi_j(y) \rangle = \langle \Psi_j(y) | \hbar V_y | \Psi_i(y) \rangle^*, \quad (\text{E11})$$

$$\langle \Psi_i(y) | \hbar V_z | \Psi_j(y) \rangle = \langle \Psi_j(y) | \hbar V_z | \Psi_i(y) \rangle^*. \quad (\text{E12})$$

Because the Hamiltonian is a real symmetric matrix, $C_{i,1m}$, $C_{i,2m}$, $C_{j,1n}$, and $C_{j,2n}$ are all reals. Then

$$\langle \Psi_i(y) | \hbar V_x | \Psi_j(y) \rangle = \langle \Psi_j(y) | \hbar V_x | \Psi_i(y) \rangle, \quad (\text{E13})$$

$$\langle \Psi_i(y) | \hbar V_y | \Psi_j(y) \rangle = -\langle \Psi_j(y) | \hbar V_y | \Psi_i(y) \rangle, \quad (\text{E14})$$

$$\langle \Psi_i(y) | \hbar V_z | \Psi_j(y) \rangle = \langle \Psi_j(y) | \hbar V_z | \Psi_i(y) \rangle. \quad (\text{E15})$$

The Fermi arc Berry curvature reads

$$\Omega_{\alpha\beta}^{\text{arc}} = -2 \sum_{i \neq \text{arc}} \frac{\text{Im} \langle \Psi_{\text{arc}} | \hbar V_{\alpha} | \Psi_i \rangle \langle \Psi_i | \hbar V_{\beta} | \Psi_{\text{arc}} \rangle}{(E_{\text{arc}} - E_i)^2}. \quad (\text{E16})$$

So $\Omega_{zx}^{\text{arc}} = 0$, Ω_{xy}^{arc} , and Ω_{yz}^{arc} are plotted as below (see Fig. 7) and we get $\Omega_{xy}(\lambda k_z, \lambda' k_x) = \Omega_{xy}(k_z, k_x)$, $\Omega_{yz}(\lambda k_z, \lambda' k_x) = \lambda \lambda' \Omega_{yz}(k_z, k_x)$ where $\lambda, \lambda' = \pm 1$.

[1] A. H. Castro Neto, F. Guinea, N. M. R. Peres, K. S. Novoselov, and A. K. Geim, *Rev. Mod. Phys.* **81**, 109 (2009).

[2] A. N. Grigorenko, M. Polini, and K. S. Novoselov, *Nat. Photonics* **6**, 749 (2012).

[3] M. Alidoust, K. Halterman, D. Pan, M. Willatzen, and J. Akola, *Phys. Rev. B* **102**, 115307 (2020).

[4] S. Xiao, T. Liu, L. Cheng, C. Zhou, X. Jiang, Z. Li, and C. Xu, *J. Lightwave Technol.* **37**, 3290 (2019).

- [5] S. Li, S.-G. Chen, S.-F. Xiao, H.-Q. Liu, J.-J. Mao, and J.-Z. Mao, *Plasmonics* **16**, 441 (2021).
- [6] D. Dong, Y. Liu, Y. Fei, Y. Fan, J. Li, Y. Feng, and Y. Fu, *Appl. Opt.* **58**, 3862 (2019).
- [7] X. Wang, Q. Ma, L. Wu, J. Guo, S. Lu, X. Dai, and Y. Xiang, *Opt. Express* **26**, 5488 (2018).
- [8] Z. K. Liu, B. Zhou, Y. Zhang, Z. J. Wang, H. M. Weng, D. Prabhakaran, S.-K. Mo, Z. X. Shen, Z. Fang, X. Dai, Z. Hussain, and Y. L. Chen, *Science* **343**, 864 (2014).
- [9] B.-J. Yang and N. Nagaosa, *Nat. Commun.* **5**, 4898 (2014).
- [10] T.-R. Chang, S.-Y. Xu, D. S. Sanchez, W.-F. Tsai, S.-M. Huang, G. Chang, C.-H. Hsu, G. Bian, I. Belopolski, Z.-M. Yu, S. A. Yang, T. Neupert, H.-T. Jeng, H. Lin, and M. Z. Hasan, *Phys. Rev. Lett.* **119**, 026404 (2017).
- [11] T. Morimoto, S. Zhong, J. Orenstein, and J. E. Moore, *Phys. Rev. B* **94**, 245121 (2016).
- [12] K. J. A. Ooi, Y. S. Ang, Q. Zhai, D. T. H. Tan, L. K. Ang, and C. K. Ong, *APL Photonics* **4**, 034402 (2019).
- [13] N. Nagaosa, T. Morimoto, and Y. Tokura, *Nat. Rev. Mater.* **5**, 621 (2020).
- [14] P. Hosur and X. Qi, *C. R. Phys.* **14**, 857 (2013).
- [15] A. A. Burkov, *Nat. Mater.* **15**, 1145 (2016).
- [16] B. Yan and C. Felser, *Annu. Rev. Condens. Matter Phys.* **8**, 337 (2017).
- [17] X. Wan, A. M. Turner, A. Vishwanath, and S. Y. Savrasov, *Phys. Rev. B* **83**, 205101 (2011).
- [18] G. Xu, H. Weng, Z. Wang, X. Dai, and Z. Fang, *Phys. Rev. Lett.* **107**, 186806 (2011).
- [19] H. Weng, C. Fang, Z. Fang, B. A. Bernevig, and X. Dai, *Phys. Rev. X* **5**, 011029 (2015).
- [20] S.-Y. Xu, I. Belopolski, N. Alidoust, M. Neupane, G. Bian, C. Zhang, R. Sankar, G. Chang, Z. Yuan, C.-C. Lee, S.-M. Huang, H. Zheng, J. Ma, D. S. Sanchez, B. Wang, A. Bansil, F. Chou, P. P. Shibayev, H. Lin, S. Jia *et al.*, *Science* **349**, 613 (2015).
- [21] L. X. Yang, Z. K. Liu, Y. Sun, H. Peng, H. F. Yang, T. Zhang, B. Zhou, Y. Zhang, Y. F. Guo, M. Rahn, D. Prabhakaran, Z. Hussain, S.-K. Mo, C. Felser, B. Yan, and Y. L. Chen, *Nat. Phys.* **11**, 728 (2015).
- [22] B. Q. Lv, H. M. Weng, B. B. Fu, X. P. Wang, H. Miao, J. Ma, P. Richard, X. C. Huang, L. X. Zhao, G. F. Chen, Z. Fang, X. Dai, T. Qian, and H. Ding, *Phys. Rev. X* **5**, 031013 (2015).
- [23] N. P. Armitage, E. J. Mele, and A. Vishwanath, *Rev. Mod. Phys.* **90**, 015001 (2018).
- [24] L. Wu, S. Patankar, T. Morimoto, N. L. Nair, E. Thewalt, A. Little, J. G. Analytis, J. E. Moore, and J. Orenstein, *Nat. Phys.* **13**, 350 (2017).
- [25] Y. Gao, F. Zhang, and W. Zhang, *J. Phys.: Condens. Matter* **32**, 275502 (2020).
- [26] Z.-G. Wang, Z.-G. Fu, P. Zhang, X.-G. Zhao, and W. Zhang, *Phys. Rev. B* **101**, 245313 (2020).
- [27] D. T. Son and N. Yamamoto, *Phys. Rev. Lett.* **109**, 181602 (2012).
- [28] A. Menon, S. Chattopadhyay, and B. Basu, *Phys. Rev. B* **104**, 075129 (2021).
- [29] A. A. Zyuzin, and A. A. Burkov, *Phys. Rev. B* **86**, 115133 (2012).
- [30] H.-Z. Lu, S.-B. Zhang, and S.-Q. Shen, *Phys. Rev. B* **92**, 045203 (2015).
- [31] A. A. Burkov, *J. Phys.: Condens. Matter* **27**, 113201 (2015).
- [32] P. Goswami, J. H. Pixley, and S. Das Sarma, *Phys. Rev. B* **92**, 075205 (2015).
- [33] I. Sodemann and L. Fu, *Phys. Rev. Lett.* **115**, 216806 (2015).
- [34] C. Xiao, Z. Z. Du, and Q. Niu, *Phys. Rev. B* **100**, 165422 (2019).
- [35] O. Matsyshyn and I. Sodemann, *Phys. Rev. Lett.* **123**, 246602 (2019).
- [36] Y. Gao, F. Zhang, and W. Zhang, *Phys. Rev. B* **102**, 245116 (2020).
- [37] S. Ghosh and C. Timm, *Phys. Rev. B* **99**, 075104 (2019).
- [38] S. Ghosh and C. Timm, *Phys. Rev. B* **101**, 165402 (2020).
- [39] K.-Y. Yang, Y.-M. Lu, and Y. Ran, *Phys. Rev. B* **84**, 075129 (2011).
- [40] A. A. Burkov, *Phys. Rev. Lett.* **113**, 187202 (2014).
- [41] A. C. Potter, I. Kimchi, and A. Vishwanath, *Nat. Commun.* **5**, 5161 (2014).
- [42] P. J. W. Moll, N. L. Nair, T. Helm, A. C. Potter, I. Kimchi, A. Vishwanath, and J. G. Analytis, *Nature (London)* **535**, 266 (2016).
- [43] C. Zhang, A. Narayan, S. Lu, J. Zhang, H. Zhang, Z. Ni, X. Yuan, Y. Liu, J.-H. Park, E. Zhang, W. Wang, S. Liu, L. Cheng, L. Pi, Z. Sheng, S. Sanvito, and F. Xiu, *Nat. Commun.* **8**, 1272 (2017).
- [44] C. M. Wang, H.-P. Sun, H.-Z. Lu, and X. C. Xie, *Phys. Rev. Lett.* **119**, 136806 (2017).
- [45] C. Zhang, Y. Zhang, X. Yuan, S. Lu, J. Zhang, A. Narayan, Y. Liu, H. Zhang, Z. Ni, R. Liu, E. S. Choi, A. Suslov, S. Sanvito, L. Pi, H.-Z. Lu, A. C. Potter, and F. Xiu, *Nature (London)* **565**, 331 (2019).
- [46] K. Halterman and M. Alidoust, *Opt. Express* **27**, 36164 (2019).
- [47] K. Halterman, M. Alidoust, and A. Zyuzin, *Phys. Rev. B* **98**, 085109 (2018).
- [48] T. Tamaya, T. Kato, K. Tsuchikawa, S. Konabe, and S. Kawabata, *J. Phys.: Condens. Matter* **31**, 305001 (2019).
- [49] K. Tsuchikawa, S. Konabe, T. Yamamoto, and S. Kawabata, *Phys. Rev. B* **102**, 035443 (2020).
- [50] G. Chiarello, J. Hofmann, Z. Li, V. Fabio, L. Guo, X. Chen, S. Das Sarma, and A. Politano, *Phys. Rev. B* **99**, 121401(R) (2019).
- [51] X. Jia, M. Wang, D. Yan, S. Xue, S. Zhang, J. Zhou, Y. Shi, X. Zhu, Y. Yao, and J. Guo, *New J. Phys.* **22**, 103032 (2020).
- [52] A. B. Sushkov, J. B. Hofmann, G. S. Jenkins, J. Ishikawa, S. Nakatsuji, S. Das Sarma, and H. D. Drew, *Phys. Rev. B* **92**, 241108(R) (2015).
- [53] B. Xu, Y. M. Dai, L. X. Zhao, K. Wang, R. Yang, W. Zhang, J. Y. Liu, H. Xiao, G. F. Chen, A. J. Taylor, D. A. Yarotski, R. P. Prasankumar, and X. G. Qiu, *Phys. Rev. B* **93**, 121110(R) (2016).
- [54] S. I. Kimura, H. Yokoyama, H. Watanabe, J. Sichelschmidt, V. Suss, M. Schmidt, and C. Felser, *Phys. Rev. B* **96**, 075119 (2017).
- [55] E. V. Gorbar, V. A. Miransky, I. A. Shovkovy, and P. O. Sukhachov, *Phys. Rev. B* **99**, 155120 (2019).
- [56] Z. B. Lošić, *J. Phys.: Condens. Matter* **31**, 285001 (2019).
- [57] X. Lu, D. K. Mukherjee, and M. O. Goerbig, *Phys. Rev. B* **104**, 155103 (2021).
- [58] J. Zhou, H.-R. Chang, and D. Xiao, *Phys. Rev. B* **91**, 035114 (2015).

- [59] J. Hofmann and S. Das Sarma, *Phys. Rev. B* **91**, 241108(R) (2015).
- [60] J. Hofmann and S. Das Sarma, *Phys. Rev. B* **93**, 241402(R) (2016).
- [61] Z. B. Losic, *J. Phys.: Condens. Matter* **30**, 365003 (2018).
- [62] J. C. W. Song and M. S. Rudner, *Phys. Rev. B* **96**, 205443 (2017).
- [63] G. M. Andolina, F. M. D. Pellegrino, F. H. L. Koppens, and M. Polini, *Phys. Rev. B* **97**, 125431 (2018).
- [64] F. Adinehvand, Z. Faraei, T. Farajollahpour, and S. A. Jafari, *Phys. Rev. B* **100**, 195408 (2019).
- [65] I. Panfilov, A. A. Burkov, and D. A. Pesin, *Phys. Rev. B* **89**, 245103 (2014).
- [66] E. V. Gorbar, V. A. Miransky, I. A. Shovkovy, and P. O. Sukhachov, *Phys. Rev. Lett.* **118**, 127601 (2017).
- [67] Z. Long, Y. Wang, M. Erukhimova, M. Tokman, and A. Belyanin, *Phys. Rev. Lett.* **120**, 037403 (2018).
- [68] C. Tan, Z. Yue, Z. Dai, Q. Bao, X. Wang, H. Lue, and L. Wang, *Opt. Mater.* **86**, 421 (2018).
- [69] A. Politano, G. Chiarello, B. Ghosh, K. Sadhukhan, C.-N. Kuo, C. S. Lue, V. Pellegrini, and A. Agarwal, *Phys. Rev. Lett.* **121**, 086804 (2018).
- [70] C. Wang, Y. Sun, S. Huang, Q. Xing, G. Zhang, C. Song, F. Wang, Y. Xie, Y. Lei, Z. Sun, and H. Yan, *Phys. Rev. Appl.* **15**, 014010 (2021).
- [71] R. Okugawa and S. Murakami, *Phys. Rev. B* **89**, 235315 (2014).
- [72] Z. Fang, N. Nagaosa, K. S. Takahashi, A. Asamitsu, R. Mathieu, T. Ogasawara, H. Yamada, M. Kawasaki, Y. Tokura, and K. Terakura, *Science* **302**, 92 (2003).
- [73] Q. Wang, Y. Xu, R. Lou, Z. Liu, M. Li, Y. Huang, D. Shen, H. Weng, S. Wang, and H. Lei, *Nat. Commun.* **9**, 3681 (2018).
- [74] A. L. Fetter, *Phys. Rev. B* **32**, 7676 (1985).
- [75] D. Jin, L. Lu, Z. Wang, C. Fang, J. D. Joannopoulos, M. Soljačić, L. Fu, and N. X. Fang, *Nat. Commun.* **7**, 13486 (2016).
- [76] P. Di Pietro, M. Ortolani, O. Limaj, A. Di Gaspare, V. Giliberti, F. Giorgianni, M. Brahlek, N. Bansal, N. Koirala, S. Oh, P. Calvani, and S. Lupi, *Nat. Nanotech.* **8**, 556 (2013).
- [77] B. Ghosh, P. Kumar, A. Thakur, Y. S. Chauhan, S. Bhowmick, and A. Agarwal, *Phys. Rev. B* **96**, 035422 (2017).
- [78] L.-k. Shi and J. C. W. Song, *Phys. Rev. X* **8**, 021020 (2018).
- [79] D. Xiao, M.-C. Chang, and Q. Niu, *Rev. Mod. Phys.* **82**, 1959 (2010).